www.sciencemag.org/content/364/6436/170/suppl/DC1

Supplementary Materials for

Anti–parity-time symmetry in diffusive systems

Ying Li*, Yu-Gui Peng*, Lei Han*, Mohammad-Ali Miri, Wei Li, Meng Xiao, Xue-Feng Zhu†, Jianlin Zhao, Andrea Alù, Shanhui Fan†, Cheng-Wei Qiu†

*These authors contributed equally to this work.
†Corresponding author. Email: xfzhu@hust.edu.cn (X.-F.Z.); shanhui@stanford.edu (S.F.); chengwei.qiu@nus.edu.sg (C.-W.Q.)

Published 12 April 2019, *Science* **364**, 170 (2019)
DOI: 10.1126/science.aaw6259

This PDF file includes:

Other Supplementary Materials for this manuscript include the following:
(available at www.sciencemag.org/content/364/6436/170/suppl/DC1)

Movies S1 to S3 (.mp4)

Materials and Methods

S1. APT-symmetric system for convective heat transfer

The temperature distribution $T(x,t)$ in a one-dimensional background with velocity v satisfies the convective-diffusion equation (*26*)

$$\frac{\partial T}{\partial t} = D\frac{\partial^2 T}{\partial x^2} - v\frac{\partial T}{\partial x}, \tag{S. 1}$$

where $D = \kappa/\rho c$ is the diffusivity, κ is the thermal conductivity, ρ and c are the density and heat capacity of the media. The material properties are all assumed to be temperature-independent for simplicity. This equation is dissipative, due to the first-order time-derivative. However, the advection term introduces a wave-like behaviour given that, for $D = 0$, Eq. (S. 1) reduces to a first-order wave (advection) equation. The eigenfrequencies of this system can be obtained by substituting $T(x,t) = Ae^{i(kx-\omega t)}$, which results in:

$$\omega = -iDk^2 + vk. \tag{S. 2}$$

For an arbitrary v, the system is dissipative with a complex eigenvalue, while the advection term gives rise to real eigenfrequencies with a linear dispersion (Fig. 1E).

For the coupled two channel case, we write the plane-wave solution to Eq. 1 in the main text

$$\begin{pmatrix} T_1(x,t) \\ T_2(x,t) \end{pmatrix} = \begin{pmatrix} A_1 \\ A_2 \end{pmatrix} e^{i(kx-\omega t)}. \tag{S. 3}$$

Thus, we have the eigenvalue problem $\omega\begin{pmatrix} A_1 \\ A_2 \end{pmatrix} = H\begin{pmatrix} A_1 \\ A_2 \end{pmatrix}$, which leads to the effective Hamiltonian

$$H = \begin{pmatrix} -i(k^2D + h) + kv & ih \\ ih & -i(k^2D + h) - kv \end{pmatrix}. \tag{S. 4}$$

As easily seen, H is APT-symmetric with the parity operator defined as

$$\mathcal{P} = \begin{pmatrix} 0 & 1 \\ 1 & 0 \end{pmatrix}, \tag{S. 5}$$

which swaps the two channels, while the time reversal operator $\mathcal{T}$ represents complex conjugation.

For $k^2v^2 < h^2$, $\omega_\pm$ are purely imaginary with eigenvectors $\boldsymbol{u}_\pm = \left(A_1^\pm, A_2^\pm\right)^T = \left(kv/h \pm i\sqrt{1-(kv/h)^2}, i\right)^T$. The fields in the two channels only differ by a phase, i.e., $\left|A_1^\pm\right| = \left|A_2^\pm\right|$. This scenario can be labeled as *exact APT regime*, given that under a proper normalization the eigenvectors preserve the symmetry of the Hamiltonian, i.e., $\mathcal{PT}\boldsymbol{u}_\pm = -\boldsymbol{u}_\pm$. Here, the eigenvectors can be written as $\boldsymbol{u}_- = i\left(e^{i(\pi-\phi)/2}, e^{-i(\pi-\phi)/2}\right)^T$ and $\boldsymbol{u}_+ = i\left(e^{-i\phi/2}, e^{i\phi/2}\right)^T$ with $\phi = \sin^{-1}(kv/h)$. The eigenstates can be gauged real by combining the forward and backward solutions: $(T_1, T_2)^T = e^{-i\omega t}e^{i(\pi-\phi)/2}[A\boldsymbol{u}(k)e^{ikx} + B\boldsymbol{u}(-k)e^{-ikx}]$. When $A = B = 1$, we get the two standing-wave solutions

$$(T_1, T_2) = 2e^{-i\omega t}(\cos kx\,, \pm\cos(kx \pm \phi)). \tag{S. 6}$$

The system reaches the exceptional point for $k^2v^2 = h^2$ associated with the critical velocity $v_{\mathrm{EP}} = h/|k|$, where the two eigenstates coalesce to $i\left(e^{-i\pi/4}, e^{i\pi/4}\right)^T$. When $k^2v^2 > h^2$, anti-PT-symmetry is broken, and the eigenvalues exhibit a finite real part according to Eq. 3 in the main text, which is now rewritten as $\omega_\pm = -i(k^2D + h) \pm \sqrt{k^2v^2 - h^2}$. The corresponding eigenstates are $\boldsymbol{u}_\pm = i\left(e^{-i\pi/4}e^{\pm\psi/2}, e^{i\pi/4}e^{\mp\psi/2}\right)^T$, where $\psi = \mathrm{sgn}(k)\cosh^{-1}(|k|v/h)$. Opposite to the previous case, there is a contrast between the eigenvector intensities in the two channels: while one eigenvector is mostly located in one channel, the other is located at the other channel. In addition, the two eigenstates involve a constant $\pi/2$ phase difference between the two channels. We note that the APT symmetry of the eigenvectors is lost since the APT operation interchanges the eigenvectors: $\mathcal{PT}\boldsymbol{u}_\pm = -\boldsymbol{u}_\mp$. The eigenstate of *H* is no longer an eigenstate of the PT operator and APT-symmetry is broken. One significant outcome of entering this symmetry-broken phase is that the eigenstates cannot be gauged to be real any longer, due to the rescaling coefficient e^ψ: if we still adapt the same gauge $A = B = 1$, which gives a real solution of T_1, the eigenstate becomes

$$(T_1, T_2) = e^{-i\omega t}\left(2\cos(kx), e^{-\psi}e^{i(kx+\pi/2)} + e^{\psi}e^{-i(kx+\pi/2)}\right), \quad \text{(S. 7)}$$

where in channel 2 the opposite waves have reciprocal amplitudes. The opposite waves in both channels cannot be balanced simultaneously. With the nonzero Re(ω) or eigenfrequency, no standing-wave solution exists and movement of temperature profile can be found in at least one channel.

It is worth noting the advantage of heat convection in studying APT symmetry: Re($\omega_{\pm}$) and Im($\omega_{\pm}$) are independently determined by the diffusive term (containing D) and advective term (containing v). Therefore, adjusting D and v allow independent control of the symmetric (non-Hermitian) and anti-symmetric (Hermitian) parts of the Hamiltonian. The two channels with opposite direction of flow, have v's with opposite signs. This is reminiscent of the simultaneous presence of both positive and negative energy solutions in relativistic quantum mechanics, where the negative energy solution may be considered as moving backward in time (*31*). Although moving media also introduce positive or negative frequency shifts on propagating waves (*28*, *32*), these effects are not directly useful due to the originally nonzero frequency. Effects of moving media on heat conduction have been studied (*29*), but they have been mostly used to spatio-temporally modulate the density and thermal conductivity, which induces non-reciprocity. We also note that in the relativistic regime, PT-symmetry breaking for electromagnetic waves in moving media has been considered (*33*), but the mechanism (*34*, *35*) is different from ours.

S2. Two-dimensional simulations of eigenmodes

Eq. 1 in the main text is a simplified model for the 2D system in Fig. 1C. In a 2D Cartesian coordinate (x, y) with origin at the centre of the interface of thickness d and diffusivity D_i, the full equation can be written as (*26*):

$$\frac{\partial T}{\partial t}=\begin{cases} D\left(\frac{\partial^2 T_1}{\partial x^2}+\frac{\partial^2 T_1}{\partial y^2}\right)-v\frac{\partial T_1}{\partial x}, & \frac{d}{2}\le y\le b+\frac{d}{2} \\ D_i\left(\frac{\partial^2 T_i}{\partial x^2}+\frac{\partial^2 T_i}{\partial y^2}\right), & -\frac{d}{2}<y<\frac{d}{2} \\ D\left(\frac{\partial^2 T_2}{\partial x^2}+\frac{\partial^2 T_2}{\partial y^2}\right)+v\frac{\partial T_2}{\partial x}, & -b-\frac{d}{2}\le y\le -\frac{d}{2} \end{cases}, \tag{S. 8}$$

where T_i is the temperature field on the interface. The matching conditions is:

$$\begin{cases} T_1=T_i, \kappa\frac{\partial T_1}{\partial y}=\kappa_i\frac{\partial T_i}{\partial y}, & y=\frac{d}{2} \\ T_2=T_i, \kappa\frac{\partial T_2}{\partial y}=\kappa_i\frac{\partial T_i}{\partial y}, & y=-\frac{d}{2} \end{cases} \tag{S. 9}$$

where κ_i is the thermal conductivity of the interface. It is obvious that the effective Hamiltonian corresponding to Eq. (S. 8) and (S. 9) is also APT symmetric, when the parity operator $\mathcal{P}$ is defined as the inversion in *y*-direction. The full equation is reduced to Eq. 1 in the main text by assuming that the temperature variance in *y*, i.e., $\partial^2 T/\partial y^2$ is negligible in the system. The boundary heat conduction following Eq. (S. 9) can be treated as a heat source term h_s in the two channels. Thus

$$\frac{\partial T}{\partial t}=\begin{cases} D\frac{\partial^2 T_1}{\partial x^2}-v\frac{\partial T_1}{\partial x}+\frac{h_{s1}}{\rho c}, & \frac{d}{2}\le y\le b+\frac{d}{2} \\ D\frac{\partial^2 T_2}{\partial x^2}+v\frac{\partial T_2}{\partial x}+\frac{h_{s2}}{\rho c}, & -b-\frac{d}{2}\le y\le -\frac{d}{2} \end{cases}. \tag{S. 10}$$

The heat comes from the heat flux q normal to the $y = \pm d/2$ boundary. When the channel width b is small, we can simply assume that the heat source is uniformly distributed along the channel width: $h_s = q/b$, where

$$\begin{aligned} q_1&=-\kappa\frac{\partial T_1}{\partial y}=-\kappa_i\frac{\partial T_i}{\partial y}, & y&=\frac{d}{2} \\ q_2&=\kappa\frac{\partial T_2}{\partial y}=\kappa_i\frac{\partial T_i}{\partial y}, & y&=-\frac{d}{2} \end{aligned} \tag{S. 11}$$

Since the T_i is linear with *y*, we have $\partial T_i/\partial y=\left(T_1|_{y=d/2}-T_2|_{y=-d/2}\right)/d$. Eq. (S. 10) turns out to be

$$\frac{\partial T}{\partial t} = \begin{cases} D\frac{\partial^2 T_1}{\partial x^2} - v\frac{\partial T_1}{\partial x} + \frac{\kappa_i}{\rho c}\frac{T_2 - T_1}{bd}, & \frac{d}{2} \le y \le b + \frac{d}{2} \\ D\frac{\partial^2 T_2}{\partial x^2} + v\frac{\partial T_2}{\partial x} + \frac{\kappa_i}{\rho c}\frac{T_1 - T_2}{bd}, & -b - \frac{d}{2} \le y \le -\frac{d}{2} \end{cases}, \qquad \text{(S. 12)}$$

where we assume little difference between T_1 (T_2) at the $y = d/2$ ($y = -d/2$) boundary and inside the upper (lower) channel, due to the small channel width. Eq. (S. 12) is just Eq. 1 in the main text if we define the heat exchange rate $h = \kappa_i (\rho c)^{-1}(bd)^{-1}$.

Finite-element simulations were performed using COMSOL Multiphysics®. The medium is assumed to have the diffusivity $D = 100\ \text{mm}^2/\text{s}$, which is much larger than common materials for convenience in studying and observing the transient behaviour of the system. The density and heat capacity are set as ρ = 1000 kg/m^3, and c = 1000 J/kg·K. The thin interface has thermal conductivity κ_i = 1 W/m·K. The dimensions are set as $a = 100$ mm, $b = 5$ mm, and $d = 1$ mm. For the convenience of study, we impose periodic boundary conditions at the two ends of the system and focus on the fundamental wave $k = \pm k_0 = \pm 2\pi/L = \pm a^{-1}$, which corresponds to the smallest $-\text{Im}(\omega)$ or decay rate. Critical velocity is calculated as $v_{\text{EP}} = h/|k| = \kappa_i (\rho c)^{-1}(bd)^{-1}|k|^{-1}$ = 2.0 cm/s.

The post processing of the eigenstates was carried out as follows. In COMSOL, two eigenstates will be found for each eigenvalue, which are linearly independent vectors in the space spanned by the forward and backward solutions with wave numbers $\pm k$. Therefore, we can obtain a standing-wave solution for T_1 ($2e^{\text{Im}(\omega)t}\cos kx$) by finding the appropriate linear combination of the two numerical solutions. The gauged results can then be compared with the analytical solutions Eq. (S. 6) and (S. 7) in the symmetric and symmetry broken phase, respectively.

S3. Three-dimensional simulations of transient evolutions

The interior and exterior radii of the rings are R_1 = 100 mm and R_2 = 110 mm, respectively. The velocity of the upper (lower) channel is $-\Omega r$ (Ωr), where Ω is the angular velocity and r is the distance to the centre of ring in the xy-plane. Each channel has a height of 5 mm and the thickness of the interlayer is 1 mm. Therefore, the temperatures along the upper and lower interior edges of the rings follow almost the same condition as T_1 and T_2 in the two-dimensional model, with $v = \Omega R_1$. Two different initial conditions are adopted. One is the even mode that $T = T_0 + Cy$ for the entire system, where T_0 = 293.15 K is the average temperature and C = 0.5 K/mm is the temperature gradient. The other is the odd mode that $T = T_0 \pm Cy$ in the upper and lower channels, while $T = T_0$ in the interlayer. Each simulation was performed until the maximum temperature dropped close to T_0 (within 0.1 K).

S4. Experimental observation of transient evolutions

Ring 1 and Ring 2 are made of polycaprolactam (PA6) with thermal conductivity 1.2 W/m·K and diffusivity 0.73 mm^2/s (ρc = 1.64 ×10^6 J/m^3·K). The thickness, interior and exterior radius of the rings are b = 1 mm, R_1 = 50 mm and R_2 = 55 mm, respectively. Both rings are connected to aluminium frames to be rotated. Small wood blocks (thermal conductivity 0.15 W/mK) are used to thermally insulate the rings from the frames. The grease layer has thermal conductivity κ_i = 0.11 W/m·K and thickness around d = 0.5 mm. According to the derivation following Eq. (S. 12), the heat exchange rate is $h = \kappa_i (\rho c)^{-1}(bd)^{-1}$ = 0.13 s^{-1}. Therefore, the critical rotation speed should be $v_{EP}/R_1 = h/(k_0 R_1) = h$ = 1.27 rpm. To generate temperature gradient, the bottom of the copper plate was immersed in 70 °C hot water, while the top was covered by an ice bag. The temperature fields and their evolutions were measured with a Fotric 233s infrared camera, whose imaging resolution and measurement precision are 160 × 120 pixel and 0.1 °C, respectively.

The infrared images were post processed to extract quantitative data about the temperature field. We firstly deformed the images to restore the ring to circular shape, according to which we found the centre and region of the ring in the deformed images. Since the experimentally measured temperature field contains noisy points such as temperature on the wood blocks and the frames, the maximum temperature point max(T_1) used to analyse numerical results drifts drastically in the experiments and is no longer a good choice. We then introduce the concept of temperature dipole $\boldsymbol{p}_T(t) = A^{-1}\int T(\boldsymbol{r},t)\boldsymbol{r}\mathrm{d}s$, where A is the area of the ring, $\boldsymbol{r}$ is the position vector from the ring centre, and ds is the area element. The integral is carried out on the whole ring. Similar as the electric dipole, $\boldsymbol{p}_T$ characterizes how much the temperature field is unevenly distributed on the ring. Therefore, it is a suitable quantity that represents the temperature profile. For the ideal linear temperature fields, the direction of $\boldsymbol{p}_T$ coincides with the direction of the temperature gradient. In practice, since the infrared images are pixelized, the directions of $\boldsymbol{p}_T$ can be simply calculated from the temperature-weighted averages of position vectors for pixel points on the ring.

Supplementary Text

S1. Dispersion relation

We can study the dispersion relation of the system according to Eq. 2 of the main text. For different v, the theoretical dispersion relation is plotted in Fig. S1. It is immediately seen that with an increasing wavenumber k, the system undergoes an APT-symmetry breaking similar to the v dependence in the main text.

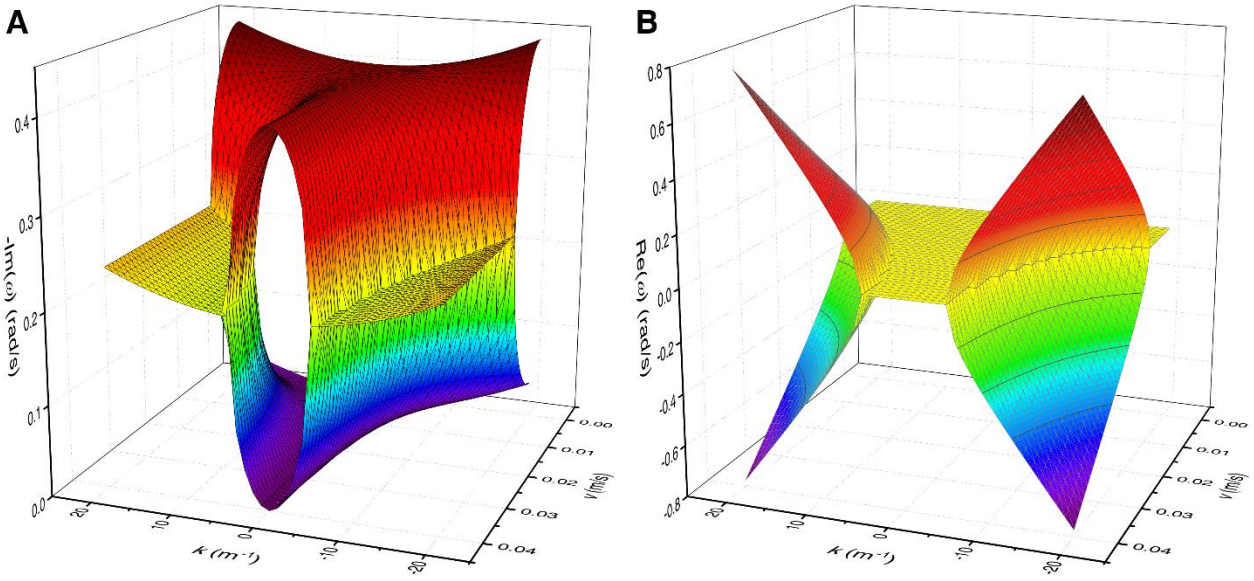

Fig. S1. Dispersion of the APT heat convection system. (**A**) Decay rate. (**B**) Eigenfrequency.

The phase transition is clearly observed by rescaling the three-dimensional model while maintaining the same background velocity. Therefore, we performed simulations with inner the radius R_1 = 125 mm and 66.7 mm and fixed v = 2.0 cm/s, the corresponding wavenumber at the EP is k_0 = 10 m^{-1}. The wavenumber of the temperature profiles is changed with the circumferences to be k = 8 m^{-1} and 15 m^{-1}. The corresponding trajectories of maximum temperature are plotted in Fig. S2. The familiar contrast between rest and motion is obvious. By performing studies with different wavenumbers, we also reconfirmed that APT symmetry is achieved in full band.

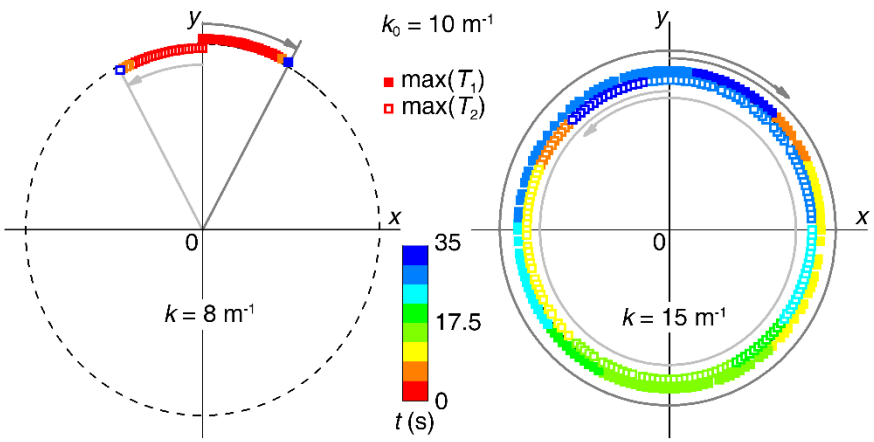

Fig. S2. Trajectories of max(T_1) and max(T_2) for different circumferences of the channels.

S2. Counter-flow propagation and direction reversal

Since the initial conditions are symmetric, the motion of fields maintains symmetry after swapping the channels and applying a spatial reflection. We can break this symmetry by using a different initial condition that the amplitude in channel 2 is smaller. We adopt the initial condition $T = T_0 + C_1 y$ in channel 1 and the interlayer while $T = T_0 - C_2 x$ in channel 2, where C_1 = 0.5 K/mm and C_2 = 0.3 K/mm. At v = 2.5 cm/s in the symmetry broken phase (Fig. S3A), we see that the chiral symmetry is also broken and the fields in both channels move in the clockwise direction, keeping a phase difference ϕ, which vibrates in a range from 0.45π to 0.6π with time (Fig. S3B). This observed behaviour can be well explained by the analytical eigenstates. Back to the one-dimensional model, we have an eigenstate of combined forward and backward waves

$$(T_1, T_2)^T = e^{-i\omega t} e^{-i\pi/4}\, e^{-\psi/2}\left[A e^{ikx}\boldsymbol{u}_+(k) + B e^{-ikx}\boldsymbol{u}_+(-k)\right], \qquad \text{(S. 13)}$$

where $\boldsymbol{u}_+(k) = i\left(e^{-i\pi/4}e^{\psi/2}, e^{i\pi/4}e^{-\psi/2}\right)^T$ and $\psi = \mathrm{sgn}(k)\cosh^{-1}(|k|v/h)$. By taking the real part, we get

$$T_j = e^{\mathrm{Im}(\omega)t}\left\{A_j \cos\left[kx - \mathrm{Re}(\omega)t + \phi_j\right] + B_j \cos[kx + \mathrm{Re}(\omega)t + \phi_j]\right\}, \qquad \text{(S. 14)}$$

where $j = 1, 2, A_1 = A, A_2 = Ae^{-\psi}, B_1 = B, B_2 = Be^{\psi}, \phi_2 - \phi_1 = \pi/2$. The maximum points can be calculated from $\partial T_j/\partial x = 0 \rightarrow \tan\left[kx_j(t) + \phi_j\right] = \tan[\mathrm{Re}(\omega)t]\,(A_j - B_j)/(A_j + B_j)$. In the 3D system, the time-dependent phase difference of maximum points is $\phi(t) = k[x_1(t) - x_2(t)]$. Therefore

$$\phi(t) = \phi_0 + \tan^{-1}\left\{\frac{M\tan[Re(\omega)t]}{1+N\tan^2[Re(\omega)t]}\right\}, \quad \text{(S. 15)}$$

where

$$M = \frac{A_1-B_1}{A_1+B_1} - \frac{A_2-B_2}{A_2+B_2}, N = \left(\frac{A_1-B_1}{A_1+B_1}\right)\left(\frac{A_2-B_2}{A_2+B_2}\right). \quad \text{(S. 16)}$$

Eq. (S. 15) represents a vibration with the frequency 2Re(ω) and average ϕ_0, which should be $\phi_2 - \phi_1 = \pi/2$ according to the theory. The simulation results fit well with this expectation, and provide a fit $\phi_0 = 0.52\pi$, close to the theoretical prediction. We can calculate the ratio $\sqrt{(A_1/B_1)/(A_2/B_2)} = 1.947$ with the fitted parameters. On the other hand, according to the theory, we have

$$\sqrt{(A_1/B_1)/(A_2/B_2)} = e^{\psi} = v/v_{\mathrm{EP}} + \sqrt{(v/v_{\mathrm{EP}})^2 - 1} = 2, \quad \text{(S. 17)}$$

which is in good agreement.

A series of simulations were performed with the same initial condition for v from 0 to 2.9 cm/s. By fitting the time-dependent phase differences of results at v = 2.05 to 2.9 cm/s with Eq. (S. 15), we can obtain a fitted value of Re(ω) and ϕ_0 for each v. For v from 0 to 2.0 cm/s, the phase differences ϕ for the stationary fields eventually reached is directly obtained. We rename ϕ_0 for v > 2.0 cm/s as ϕ and plot its value in the full range of v in Fig. S3C. The result is compared with the theory that $\phi = \arcsin(v/v_{\mathrm{EP}})$ for $v < v_{\mathrm{EP}}$ and $\phi = \pi/2$ for $v > v_{\mathrm{EP}}$. The phase difference calculated from the eigenstates for the two-dimensional model is also plotted. In the symmetry broken region, we plot the Re(ω) according to the theory, which is directly simulated for the two-dimensional

model along with the fitted values in Fig. S3D. Both figures show a good agreement among the three results. It is confirmed that an APT-symmetry breaking phase transition indeed happens, and the critical velocity is v = 2.0 cm/s.

Although a similar case can be obtained for v from 2.05 to 2.9 cm/s ($v = 2.0 + 0.002t$ (cm/s)), we can observe another change of chirality when v is dynamically increased as in Fig. S3E. The dynamically changed parameter would not allow an adjustment of gauge for the system and results in a U-turn of the field in channel 2 at t = 31 s. This direction reversal phenomenon is a clear demonstration of the effect of dynamically evolving non-Hermitian Hamiltonian, which may become quite different than the one in the adiabatic case (*36–40*).

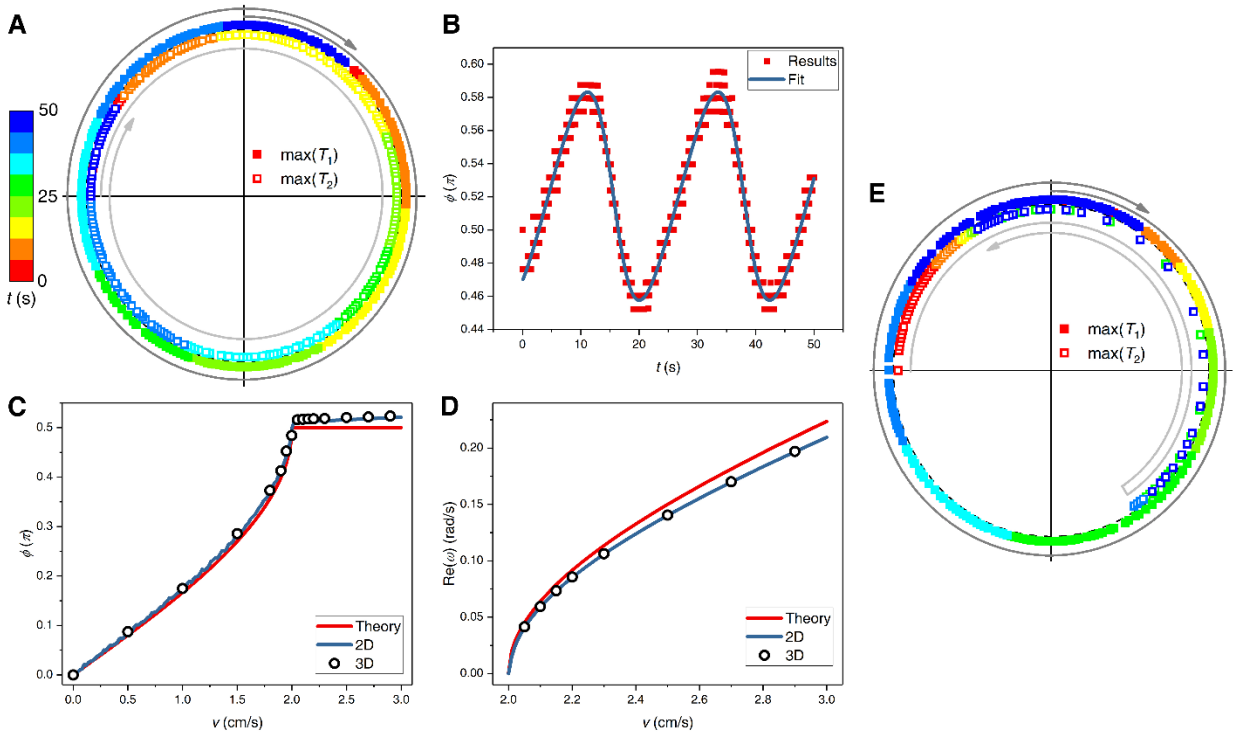

Fig. S3. Results with asymmetric initial condition. (**A**) The temperature profiles in both channels move clockwise, one following while one against the background motion. The trajectories are plotted for v = 2.5 cm/s. (**B**) The phase difference between two profiles is relatively stable and

varies in a small range between 0.45π to 0.6π with a frequency which should be two times the eigenfrequency of the system according to theory. The phase evolution can be fitted to theory well and can help determine the phase difference between forward waves in each channel as well as the eigenfrequency in the APT-symmetry broken phase. (**C**) The phase differences show a clear pattern of phase transition, similar to the pattern of the $-\mathrm{Im}(\omega)$. Those obtained from transient results of the three-dimensional system are almost precisely on the curve obtained from the eigenstates of the two-dimensional system. They are also close to the theoretical prediction. (**D**) Nonzero eigenfrequency emerges after crossing the critical velocity. Again, the two results are in good accordance with each other and the theory. (**E**) Dynamically increasing v from 2.0 to 3.0 cm/s, a direction reversal from clockwise to counter clockwise motion occurs for the profile in channel 2 as indicated with the light grey arrowed curve.

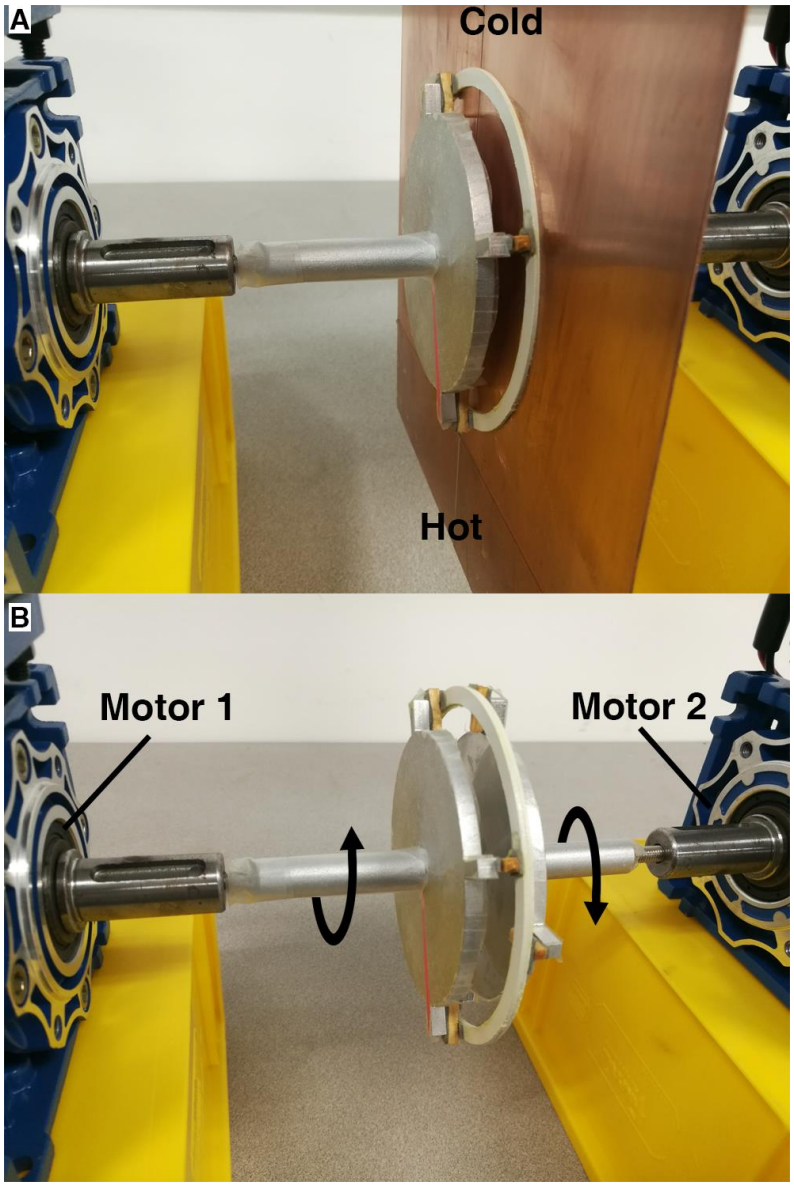

Fig. S4. Photos of the experimental setup. (**A**) Launching the temperature gradient. (**B**) Performing measurements.

Movie S1.

Evolution of temperature profiles on Ring 1. The left parts are the results of the system. The right parts are the result of the reference (simply an uncoupled Ring 1). The rotation speeds of the Rings are 0.5 rpm.

Movie S2.

Same as Movie S1. Rotation speeds are 1.0 rpm.

Movie S3.

Same as Movie S1. Rotation speeds are 1.5 rpm.

References and Notes

1. C. M. Bender, S. Boettcher, Real spectra in non-Hermitian Hamiltonians having PT symmetry. *Phys. Rev. Lett.* **80**, 5243–5246 (1998). doi:10.1103/PhysRevLett.80.5243

2. C. M. Bender, Making sense of non-Hermitian Hamiltonians. *Rep. Prog. Phys.* **70**, 947–1018 (2007). doi:10.1088/0034-4885/70/6/R03

3. K. G. Makris, R. El-Ganainy, D. N. Christodoulides, Z. H. Musslimani, Beam dynamics in PT symmetric optical lattices. *Phys. Rev. Lett.* **100**, 103904 (2008). doi:10.1103/PhysRevLett.100.103904 Medline

4. C. E. Rüter, K. G. Makris, R. El-Ganainy, D. N. Christodoulides, M. Segev, D. Kip, Observation of parity–time symmetry in optics. *Nat. Phys.* **6**, 192–195 (2010). doi:10.1038/nphys1515

5. B. Peng, Ş. K. Özdemir, F. Lei, F. Monifi, M. Gianfreda, G. L. Long, S. Fan, F. Nori, C. M. Bender, L. Yang, Parity-time-symmetric whispering-gallery microcavities. *Nat. Phys.* **10**, 394–398 (2014). doi:10.1038/nphys2927

6. X. Zhu, H. Ramezani, C. Shi, J. Zhu, X. Zhang, PT-Symmetric Acoustics. *Phys. Rev. X* **4**, 031042 (2014). doi:10.1103/PhysRevX.4.031042

7. R. El-Ganainy, K. G. Makris, M. Khajavikhan, Z. H. Musslimani, S. Rotter, D. N. Christodoulides, Non-Hermitian physics and PT symmetry. *Nat. Phys.* **14**, 11–19 (2018). doi:10.1038/nphys4323

8. W. D. Heiss, The physics of exceptional points. *J. Phys. Math. Gen.* **45**, 444016 (2012). doi:10.1088/1751-8113/45/44/444016

9. B. Peng, S. K. Özdemir, S. Rotter, H. Yilmaz, M. Liertzer, F. Monifi, C. M. Bender, F. Nori, L. Yang, Loss-induced suppression and revival of lasing. *Science* **346**, 328–332 (2014). doi:10.1126/science.1258004 Medline

10. A. Guo, G. J. Salamo, D. Duchesne, R. Morandotti, M. Volatier-Ravat, V. Aimez, G. A. Siviloglou, D. N. Christodoulides, Observation of PT-symmetry breaking in complex optical potentials. *Phys. Rev. Lett.* **103**, 093902 (2009). doi:10.1103/PhysRevLett.103.093902 Medline

11. L. Chang, X. Jiang, S. Hua, C. Yang, J. Wen, L. Jiang, G. Li, G. Wang, M. Xiao, Parity-time symmetry and variable optical isolation in active-passive-coupled microresonators. *Nat. Photonics* **8**, 524–529 (2014). doi:10.1038/nphoton.2014.133

12. Z. Lin, H. Ramezani, T. Eichelkraut, T. Kottos, H. Cao, D. N. Christodoulides, Unidirectional invisibility induced by PT-symmetric periodic structures. *Phys. Rev. Lett.* **106**, 213901 (2011). doi:10.1103/PhysRevLett.106.213901 Medline

13. A. Regensburger, C. Bersch, M.-A. Miri, G. Onishchukov, D. N. Christodoulides, U. Peschel, Parity-time synthetic photonic lattices. *Nature* **488**, 167–171 (2012). doi:10.1038/nature11298 Medline

14. L. Feng, Y.-L. Xu, W. S. Fegadolli, M.-H. Lu, J. E. B. Oliveira, V. R. Almeida, Y.-F. Chen, A. Scherer, Experimental demonstration of a unidirectional reflectionless parity-time

metamaterial at optical frequencies. *Nat. Mater.* **12**, 108–113 (2013). doi:10.1038/nmat3495 Medline

15. Z. J. Wong, Y.-L. Xu, J. Kim, K. O'Brien, Y. Wang, L. Feng, X. Zhang, Lasing and anti-lasing in a single cavity. *Nat. Photonics* **10**, 796–801 (2016). doi:10.1038/nphoton.2016.216

16. L. Feng, Z. J. Wong, R.-M. Ma, Y. Wang, X. Zhang, Single-mode laser by parity-time symmetry breaking. *Science* **346**, 972–975 (2014). doi:10.1126/science.1258479 Medline

17. H. Hodaei, M.-A. Miri, M. Heinrich, D. N. Christodoulides, M. Khajavikhan, Parity-time-symmetric microring lasers. *Science* **346**, 975–978 (2014). doi:10.1126/science.1258480 Medline

18. S. Assawaworrarit, X. Yu, S. Fan, Robust wireless power transfer using a nonlinear parity-time-symmetric circuit. *Nature* **546**, 387–390 (2017). doi:10.1038/nature22404 Medline

19. M.-A. Miri, A. Alù, Exceptional points in optics and photonics. *Science* **363**, eaar7709 (2019). doi:10.1126/science.aar7709 Medline

20. J.-H. Wu, M. Artoni, G. C. La Rocca, Non-Hermitian degeneracies and unidirectional reflectionless atomic lattices. *Phys. Rev. Lett.* **113**, 123004 (2014). doi:10.1103/PhysRevLett.113.123004 Medline

21. J.-H. Wu, M. Artoni, G. C. La Rocca, Parity-time-antisymmetric atomic lattices without gain. *Phys. Rev. A* **91**, 033811 (2015). doi:10.1103/PhysRevA.91.033811

22. P. Peng, W. Cao, C. Shen, W. Qu, J. Wen, L. Jiang, Y. Xiao, Anti-parity-time symmetry with flying atoms. *Nat. Phys.* **12**, 1139–1145 (2016). doi:10.1038/nphys3842

23. Y. Choi, C. Hahn, J. W. Yoon, S. H. Song, Observation of an anti-PT-symmetric exceptional point and energy-difference conserving dynamics in electrical circuit resonators. *Nat. Commun.* **9**, 2182 (2018). doi:10.1038/s41467-018-04690-y Medline

24. V. V. Konotop, D. A. Zezyulin, Odd-Time Reversal PT Symmetry Induced by an Anti-PT-Symmetric Medium. *Phys. Rev. Lett.* **120**, 123902 (2018). doi:10.1103/PhysRevLett.120.123902 Medline

25. F. Yang, Y.-C. Liu, L. You, Anti-PT symmetry in dissipatively coupled optical systems. *Phys. Rev. A* **96**, 053845 (2017). doi:10.1103/PhysRevA.96.053845

26. A. Bejan, *Convection Heat Transfer* (Wiley, 2013).

27. S. Franke-Arnold, G. Gibson, R. W. Boyd, M. J. Padgett, Rotary photon drag enhanced by a slow-light medium. *Science* **333**, 65–67 (2011). doi:10.1126/science.1203984 Medline

28. R. Fleury, D. L. Sounas, C. F. Sieck, M. R. Haberman, A. Alù, Sound isolation and giant linear nonreciprocity in a compact acoustic circulator. *Science* **343**, 516–519 (2014). doi:10.1126/science.1246957 Medline

29. D. Torrent, O. Poncelet, J.-C. Batsale, Nonreciprocal Thermal Material by Spatiotemporal Modulation. *Phys. Rev. Lett.* **120**, 125501 (2018). doi:10.1103/PhysRevLett.120.125501 Medline

30. Y. Li, K.-J. Zhu, Y.-G. Peng, W. Li, T. Yang, H.-X. Xu, H. Chen, X.-F. Zhu, S. Fan, C.-W. Qiu, Thermal meta-device in analogue of zero-index photonics. *Nat. Mater.* **18**, 48–54 (2019). doi:10.1038/s41563-018-0239-6 Medline

31. R. P. Feynman, The Theory of Positrons. *Phys. Rev.* **76**, 749–759 (1949). doi:10.1103/PhysRev.76.749

32. R. Huang, A. Miranowicz, J.-Q. Liao, F. Nori, H. Jing, Nonreciprocal Photon Blockade. *Phys. Rev. Lett.* **121**, 153601 (2018). doi:10.1103/PhysRevLett.121.153601 Medline

33. M. G. Silveirinha, Spontaneous parity-time-symmetry breaking in moving media. *Phys. Rev. A* **90**, 013842 (2014). doi:10.1103/PhysRevA.90.013842

34. M. G. Silveirinha, Optical Instabilities and Spontaneous Light Emission by Polarizable Moving Matter. *Phys. Rev. X* **4**, 031013 (2014). doi:10.1103/PhysRevX.4.031013

35. T. A. Morgado, M. G. Silveirinha, Negative Landau Damping in Bilayer Graphene. *Phys. Rev. Lett.* **119**, 133901 (2017). doi:10.1103/PhysRevLett.119.133901 Medline

36. J. Doppler, A. A. Mailybaev, J. Böhm, U. Kuhl, A. Girschik, F. Libisch, T. J. Milburn, P. Rabl, N. Moiseyev, S. Rotter, Dynamically encircling an exceptional point for asymmetric mode switching. *Nature* **537**, 76–79 (2016). doi:10.1038/nature18605 Medline

37. H. Xu, D. Mason, L. Jiang, J. G. E. Harris, Topological energy transfer in an optomechanical system with exceptional points. *Nature* **537**, 80–83 (2016). doi:10.1038/nature18604 Medline

38. A. U. Hassan, B. Zhen, M. Soljačić, M. Khajavikhan, D. N. Christodoulides, Dynamically Encircling Exceptional Points: Exact Evolution and Polarization State Conversion. *Phys. Rev. Lett.* **118**, 093002 (2017). doi:10.1103/PhysRevLett.118.093002 Medline

39. X.-L. Zhang, S. Wang, B. Hou, C. T. Chan, Dynamically Encircling Exceptional Points: In situ Control of Encircling Loops and the Role of the Starting Point. *Phys. Rev. X* **8**, 021066 (2018). doi:10.1103/PhysRevX.8.021066

40. J. W. Yoon, Y. Choi, C. Hahn, G. Kim, S. H. Song, K.-Y. Yang, J. Y. Lee, Y. Kim, C. S. Lee, J. K. Shin, H.-S. Lee, P. Berini, Time-asymmetric loop around an exceptional point over the full optical communications band. *Nature* **562**, 86–90 (2018). doi:10.1038/s41586-018-0523-2 Medline